Energy Advances

ROYAL SOCIETY OF CHEMISTRY

PAPER

View Article Online
View Journal

Cite this: DOI: 10.1039/d6ya00077k

Effects of operating temperature on kinetics and performance of iron/iron redox flow batteries

Challuri Sai Venkata Akhil Kumar, *[ab] Arghyadeep De, [f] Hubert Weyrauch,[a] Jens Tübke [ab] and Jens Noack [acde]

The all-iron redox flow battery (IRFB) offers a promising low-cost solution for large-scale energy storage; however, its performance is compromised by parasitic reactions, particularly hydrogen evolution. The impact of operating temperature on lab-scale cell performance is a critical yet underexplored area. This study systematically examines the influence of temperature on an IRFB utilizing a 1.5 M $FeCl_2$, 2 M NH_4Cl, and 0.2 M HCl electrolyte. Electrochemical characterization was performed over the temperature range of 20–80 °C, while lab-scale cell cycling stability was assessed over 20–50 °C. Electrochemical analysis indicated that elevated temperatures significantly enhance reaction kinetics, as evidenced by a nearly fivefold increase in the diffusion coefficient of the Fe^{2+}/Fe^{3+} redox couple, rising from 1.89×10^{-6} cm^2 s^{-1} at 20 °C to 8.93×10^{-6} cm^2 s^{-1} at 80 °C. Morphological studies further revealed improved and more uniform iron deposition at higher temperatures. Nonetheless, initial battery cycling revealed that while kinetics improved, maintaining a temperature of 50 °C resulted in rapid performance degradation and electrolyte precipitation, driven by accelerated hydrogen evolution and subsequent pH shifts. An optimal operating temperature of 40 °C was identified, effectively balancing kinetic advantages with manageable side reactions. To enhance long-term stability, a soft-start cycling protocol was introduced, beginning cycles at 20 °C before ramping the temperature to 40 °C. This approach successfully reduced early-stage hydrogen losses and more than doubled the stable operational lifetime to over 80 cycles. Extended validation under high-capacity constant current constant voltage (CCCV) conditions, with *in situ* monitoring, confirmed that this protocol induces a self-stabilizing effect, characterized by a progressive reduction in parasitic hydrogen evolution currents and robust tolerance to negolyte pH excursions beyond the critical precipitation threshold at pH 3. Under these optimized conditions, the battery achieved a coulombic efficiency of 94%, a voltaic efficiency of 63%, and an energy efficiency of 60% at a current density of 25 mA cm^{-2}. These findings highlight the crucial role of thermal management in IRFB systems and present a viable strategy for enhancing their efficiency and long-term cyclability.

Received 13th March 2026,
Accepted 8th June 2026

DOI: 10.1039/d6ya00077k

rsc.li/energy-advances

Introduction

The global imperative to transition towards renewable energy sources, such as solar and wind, has exposed a critical vulnerability: their inherent intermittency.[1,2] To ensure grid stability and bridge the gap between fluctuating supply and continuous demand, the development of reliable, scalable, and cost-effective large-scale energy storage systems (ESS) is paramount.[3,4] Among the diverse ESS technologies, redox flow batteries (RFBs) have emerged as an exceptionally promising solution for grid-scale applications.[5,6] Distinguished by their unique architecture that decouples energy capacity from power output, RFBs allow for the independent scaling of energy (*via* electrolyte volume) and power (*via* the electrochemical stack size).[7,8] This modularity, combined with a long cycle life, high safety, and minimal self-discharge, makes RFBs ideal for

[a] *Applied Electrochemistry, Fraunhofer Institute for Chemical Technology ICT, 76327 Pfinztal, Germany*
[b] *Karlsruhe Institute of Technology (KIT) Institute for Mechanical Process Engineering and Mechanics, Geb. 30.70, Straße am Forum 8, 76131, Karlsruhe, Germany*
[c] *Australian Institute for Bioengineering and Nanotechnology, The University of Queensland (UQ), Brisbane, QLD, 4072, Australia*
[d] *Universität der Bundeswehr München, Fakultät elektrische Energiesysteme und Informationstechnik (EIT), Werner-Heisenberg-Weg 39, 85579, Neubiberg, Germany*
[e] *German Australian Alliance for Electrochemical Technologies for Storage of Renewable Energy (CENELEST), University of New South Wales (UNSW), Australia*
[f] *Friedrich-Alexander-Universität Erlangen-Nürnberg, Lehrstuhl für Elektrische Energietechnik, Fürther Str. 250, 90429, Nürnberg, Germany*

long-duration energy storage.[9,10] However, the commercial frontrunner, the all-vanadium RFB (VRFB), has its widespread adoption constrained by the high and volatile cost of vanadium, which has motivated intensive research into systems based on more earth-abundant and economical elements.[11,12] In this context, the all-iron redox flow battery (IRFB) has garnered significant attention as a compelling alternative, leveraging the low cost, low toxicity, and natural abundance of iron to offer a pathway toward economically viable grid storage.[13,14]

The fundamental electrochemistry of the IRFB is based on the reversible redox reactions of iron in three different oxidation states. During the charging process, ferrous ions (Fe^{2+}) in the positive half-cell (posolyte) are oxidized to ferric ions (Fe^{3+}). Simultaneously, in the negative half-cell (negolyte), Fe^{2+} ions are reduced and plated as a layer of metallic iron (Fe^0) onto the electrode surface. The process is reversed during discharge.[15] The standard half-cell reactions are as follows:

$$Fe^{2+}_{(aq)} \rightleftharpoons Fe^{3+}_{(aq)} + e^- \quad \varphi^{0,+} = +0.77\ V \qquad (1)$$

$$Fe^{2+}_{(aq)} + 2e^- \rightleftharpoons Fe_{(s)} \quad \varphi^{0,-} = -0.44\ V \qquad (2)$$

$$3\ Fe^{2+}_{(aq)} \rightleftharpoons Fe_{(s)} + 2Fe^{3+}_{(aq)} \quad \varphi_{cell} = 1.21\ V \qquad (3)$$

The operating mechanism of all-iron redox flow batteries differs significantly from that of conventional all-liquid redox flow batteries due to the solid–liquid phase transition at the negative electrode.[15] However, despite its compelling advantages, the practical implementation of the IRFB is beset by several significant electrochemical and operational challenges. The most dominant of these is the parasitic hydrogen evolution reaction (HER), which occurs at the negative electrode, particularly in acidic electrolytes (pH < 2) required to maintain iron solubility.[16,17] The standard potential for iron deposition (-0.44 V) is more negative than that of the hydrogen evolution reaction (0 V), making HER a thermodynamically favorable competing reaction during the charging phase.[18,19] This parasitic reaction has multiple detrimental consequences. Firstly, it directly consumes charge that would otherwise be used for iron plating, thereby significantly reducing the battery's coulombic efficiency.[20] Secondly, the continuous consumption of protons (H^+) from the negolyte causes its pH to increase gradually. As illustrated by the Pourbaix diagram for iron, an increase in pH beyond a critical threshold (typically >2–3) leads to the precipitation of iron hydroxides, such as $Fe(OH)_2$ and $Fe(OH)_3$.[21,22] This precipitation is catastrophic for the system, as the solid particles can clog the porous structure of the electrodes, foul the anion-exchange membrane and electrode, ultimately lead to a complete and irreversible cell failure.[23] Furthermore, the loss of hydrogen gas and iron species in the form of precipitates because of pH shift causes a permanent loss of capacity unless an efficient recombination system is in place.[24]

To address these challenges, research has focused on a holistic approach that combines materials science and systems engineering. Strategies include using electrolyte additives like tin or bismuth salts to kinetically suppress HER, as well as developing advanced 3D electrodes and selective membranes to improve plating morphology and reduce parasitic reactions.[24–26] However, since eliminating HER is difficult, the most critical innovation has been the integration of a hydrogen rebalancing system to manage its consequences. Pioneering work by Savinell's group and others demonstrated the feasibility of capturing the evolved H_2 and electrochemically reacting it with ferric ions to restore the electrolyte's pH and composition, preventing irreversible capacity loss.[13,27] This is typically achieved in a separate recombination cell where the following reactions occur:

$$2Fe^{3+}_{(aq)} + e^- \rightarrow 2Fe^{2+}_{(aq)} \quad \varphi^{0,+} = +0.77\ V \qquad (4)$$

$$2H^+_{(aq)} + 2e^- \rightarrow H_{2(g)} \quad \varphi^{0,-} = 0\ V \qquad (5)$$

$$H_{2(g)} + 2Fe^{3+}_{(aq)} \rightarrow 2H^+_{(aq)} + 2Fe^{2+}_{(aq)} \quad \varphi_{cell} = 0.77\ V \qquad (6)$$

Building on this, research by Noack *et al.* has been pivotal in designing and optimizing these rebalance cells to operate effectively even at low hydrogen concentrations, directly addressing the capacity fade associated with long-term cycling.[28,29] While this combination of strategies is essential, the efficacy of each component is strongly dependent on operating temperature. Temperature directly influences the kinetics of the desired iron plating, the parasitic HER, and the crucial recombination reactions, as well as the stability of additives and cell materials. Understanding this complex interplay is therefore vital, yet the performance of a fully integrated IRFB system under varied thermal conditions remains largely unexplored.

Operating temperature is a critical, double-edged parameter across all RFB chemistries. In all-vanadium systems, for example, higher temperatures (*e.g.*, up to 40–50 °C) are known to improve reaction kinetics and lower electrolyte viscosity, thereby increasing voltage efficiency and peak power density.[30,31] However, these benefits are often offset by the accelerated thermal precipitation of V_2O_5 in the positive electrolyte, increased ion crossover through the membrane, which reduces coulombic efficiency, and faster degradation of cell components.[32–34] Similarly, in zinc–bromine flow batteries, temperature influences zinc plating morphology and the stability of the bromine-complexing agents essential for safe operation.[35] For the emerging class of aqueous organic RFBs, thermal stability is a primary concern, as elevated temperatures can trigger irreversible decomposition of the redox-active molecules, leading to rapid capacity fade.[36,37] This consistent trade-off between enhanced kinetics and material instability in other RFB systems underscores the universal importance of thermal management. For the IRFB, where a solid–liquid phase transition is coupled with a parasitic gas-evolution reaction, this interplay is expected to be even more complex and crucial to stable operation.

Previous work has suggested that operating IRFBs at elevated temperatures could be beneficial. Foundational work by Hruska and Savinell first suggested this, reporting a coulombic efficiency of 90% at 60 °C in an electrolytic bath, a significant improvement over room-temperature performance.[13] Jayathilake *et al.* reinforced this hypothesis by conducting a comprehensive study on the iron–chloride system. Their findings demonstrated that increasing temperature enhances ionic

conductivity and reduces both ohmic resistance (R_s) and polarization resistance (R_p), as evidenced by Nyquist plot analysis.[38] Crucially, they reported that the kinetics of iron deposition become more favorable relative to HER at higher temperatures and that the resulting metal deposit is less stressed and less prone to detachment. In a complementary study focusing specifically on the negative half-cell reactions using a rotating disk electrode (RDE), Noack *et al.* further validated these findings, achieving a coulombic efficiency of 93% at a temperature of 80 °C.[28]

While these studies provide compelling evidence of the potential benefits of thermal management, a significant gap persists in the literature. These findings are predominantly based on half-cell experiments, RDE setups, or analyses in idealized electrochemical baths. There is a noticeable lack of systematic investigation into the performance, long-term stability, and operational trade-offs of a complete, full-cell IRFB system operating across a range of temperatures under practical charge–discharge cycling conditions. The cumulative and interactive effects of temperature on hydrogen management, pH stability, precipitation onset, and overall system efficiency over extended periods have not been thoroughly characterized. It is unknown whether the kinetic benefits observed in half-cell studies will translate to stable, long-term performance in a lab-scale cell, or if accelerated degradation pathways will negate them.

This study aims to bridge that critical gap by providing the first comprehensive performance analysis of a lab-scale all-iron redox flow battery, continuously cycled over a range of operating temperatures (20–50 °C). By systematically evaluating the battery's electrochemical response, cycling stability, and key efficiency metrics, we seek to identify an optimal thermal operating window that balances kinetic advantages with long-term stability. Furthermore, we introduce a "soft start" operational protocol as a practical strategy to mitigate initial inefficiencies and significantly enhance the long-term cyclability and viability of the all-iron redox flow battery system.

Experimental methods

Electrolyte preparation

The chemical stability of the electrolyte is crucial for investigating the intrinsic kinetics of the Fe/Fe^{2+} redox couple. The electrolyte was prepared by dissolving Iron(II) chloride tetrahydrate ($FeCl_2{\cdot}4H_2O$, ≥99%, Carl Roth GmbH), ammonium chloride (NH_4Cl, ≥99.7%, Carl Roth GmbH), and hydrochloric acid (HCl, 37%, ITW Reagents) in ultrapure water (55 μS cm^{-1}) to achieve a final concentration of 1.5 M $FeCl_2$, 2 M NH_4Cl, and 0.2 M HCl. All reagents were utilized as received, without further purification. The solution was purged with nitrogen for 15 minutes to ensure deoxygenation and was used within 24 hours of preparation to guarantee chemical stability.

Experimental setup and cell configuration

The electrolyte tanks of the iron/iron redox flow battery were filled with a 1:1 volume ratio of the prepared electrolyte, consisting of 1.5 M $FeCl_2$, 2 M NH_4Cl, and 0.2 M HCl. A custom-built test stand was established for electrochemical characterization, as depicted in the schematic diagram in Fig. 1(a). The system architecture consisted of the main iron/iron redox flow cell, an iron/hydrogen recombination cell, and two intermediate storage tanks. A dual-line peristaltic pump circulated the electrolyte, while a Gamry Reference

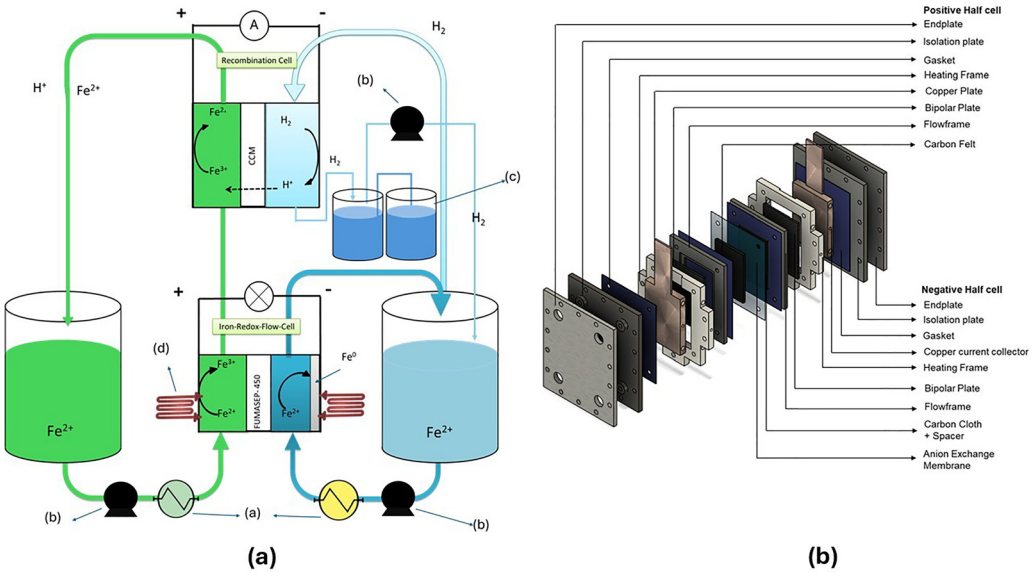

Fig. 1 Experimental configuration. (a) Schematic diagram of the iron/iron redox flow battery (IRFB) test stand, illustrating the dual-circuit design with the integrated hydrogen management and recombination loop: (a) heating hoses, (b) electrolyte circulation pumps, (c) back-pressure water tanks, and (d) cartridge heaters. (b) Exploded view of the single-cell architecture, detailing the flow frames, copper current collectors with embedded heaters, electrodes, and the custom 3D-printed spacer used in the negative half-cell.

3000 potentiostat (Gamry Instruments, USA) controlled the electrochemical cycling and analysis. To actively manage the gaseous byproducts, the fluidic network was configured such that gaseous hydrogen from the negative storage tank's headspace was purged directly into the inlet of the recombination cell's negative half-cell. The output of the positive energy storage medium (Fe^{3+}/Fe^{2+}) was connected to the input of the positive half-cell of the recombination cell to provide the necessary oxidant. After passing through the recombination cell, the electrolyte was returned to the positive storage tank. A 100 mm-high water column closed the outlet connection of the recombination cell to maintain a slight positive pressure. At the same time, excess hydrogen collected in a back-pressure tank was actively recycled to the negative storage tank to maintain the acidic atmosphere (hydrogen recycling technique).

The main iron/iron redox flow cell, illustrated in Fig. 1(b), comprised two half-cells with an active area of 40 cm^2, separated by an anion-exchange membrane (FUMASEP FAP-450, Fumatech GmbH, Germany). Both half-cells consisted of a polyvinyl chloride (PVC) flow frame embedded with a 3-mm-thick graphite bipolar plate (Schunk Group, Germany) for electrical contact. The gap between the frame and the carbon plate was sealed with conventional silicone sealant. A thermally treated carbon felt (GFA 4.6 EA, SGL Carbon, Germany) was positioned within the positive half-cell flow frame in a flow-through configuration, allowing the electrolyte to permeate the electrode and maximizing the electrochemical surface area. Conversely, the negative half-cell employed a flow-by design to accommodate solid iron deposition without clogging. A substrate material formed of carbon fabric (ACC-507-20, Kynol Europa GmbH) was positioned within the flow frame. Crucially, a custom 3D-printed spacer was integrated into this frame to define the plating cavity. This spacer, fabricated from chemically resistant acrylonitrile butadiene styrene (ABS), featured a grid-like structure (87 mm × 62 mm) with a total height of 3.5 mm, creating an effective cavity thickness of approximately 3.3–3.4 mm. This geometry was essential for regulating uniform electrolyte distribution and providing mechanical stabilization for the growing iron deposit.

To ensure robust sealing and electrical connectivity, gasket seals were employed between all layers, and thin copper sheets served as current collectors on both ends. This setup integrated precise thermal regulation; the copper plates were modified to house embedded cartridge heaters, while heating hoses were wrapped around the electrolyte piping. PT-100 sensors monitored the temperatures of the cell body and the electrolyte, which were controlled by a PID controller to maintain the target operating temperature (20–50 °C) within ±1 °C. The complete IRFB cell was compressed between two end plates, secured by 13 screws inserted into the perimeter holes and tightened with nuts to ensure uniform contact pressure.

The recombination cell was constructed similarly to the main cell but adapted for gas diffusion. It consisted of two half-cells separated by a one-sided catalyst-coated membrane (CCM) (NAFION 115, 1 mg cm^{-2} Pt/C, baltic fuel cells, Germany), with the catalyst layer facing the negative half-cell where hydrogen oxidation occurred. Two Toray carbon papers and a glassy carbon foam (ERG Aerospace, USA) were placed in the negative cavity to establish electrical contact between the catalyst layer and the bipolar plate. At the same time, the positive half-cell utilized the same thermally treated carbon felt as the main cell. The recombination cell was electrically short-circuited to operate passively, continuously converting evolved hydrogen back into protons to maintain system pH stability. Crucially, the current generated by this electrochemical recombination reaction was continuously recorded throughout the experiments to serve as a quantitative, real-time indicator of conversion rate within the system.

Electrochemical characterization

Electrochemical analyses were conducted using a potentiostat (Modulab XM, Solartron Analytical) in a three-electrode glass cell. A 3 mm diameter graphite rod (area = 0.07 cm^2) served as the working electrode, a platinum wire as the counter electrode, and an Ag/AgCl electrode (3 M NaCl, + 0.195 V *vs.* RHE) as the reference.

Cyclic voltammetry (CV). To investigate the temperature-dependent reaction kinetics and mass transport properties of the iron redox species, cyclic voltammetry (CV) was performed across a temperature range of 20 °C to 80 °C. The applied potential was swept between −1.1 V and +0.75 V *vs.* Ag/AgCl to capture both the Fe^{2+}/Fe^{3+} (positive) and Fe^{2+}/Fe (negative) redox couples. Scans were recorded at a scan rate of 20 mV s^{-1}. To ensure the system reached a steady state and to eliminate initial transient effects, three consecutive cycles were run for each measurement, with data analysis focused on the stable second cycle.

Linear sweep voltammetry (LSV). To quantify the coulombic efficiency of the iron plating/stripping process and isolate the competition between iron deposition and the parasitic hydrogen evolution reaction (HER), linear sweep voltammetry (LSV) was employed. The protocol utilized a sequence to simulate plating conditions, beginning with an initial potentiostatic step at −1.2 V for 60 seconds to establish a stable iron nucleation layer on the graphite substrate. This was immediately followed by a cathodic linear sweep from open circuit voltage (OCV) to −1.2 V to characterize the deposition currents. Subsequently, an anodic linear sweep was performed from OCV to +0.35 V at 20 mV s^{-1} to strip the deposited iron. The ratio of the integrated anodic charge (stripping) to the cathodic charge (deposition) provided a direct measurement of the coulombic efficiency at various temperatures.

Iron deposition morphology

The microstructural evolution of the iron deposits was examined by performing potentiostatic deposition on a partially tape-masked graphite rod. The electrode was held at a potential of −1.2 V in the electrolyte for a fixed duration to grow a representative iron film. These deposition experiments were conducted at temperatures ranging from 20 °C to 50 °C. The resulting surface topology, grain structure, and roughness were subsequently analyzed using optical and laser scanning

microscopy to correlate morphological changes with the electrochemical performance data.

Battery cycling protocol

To ensure the reproducibility and reliability of the electrochemical performance data, a rigorous testing protocol was followed. Each temperature condition (20 °C, 30 °C, 40 °C, and 50 °C) was investigated in duplicate to ensure statistical validity, with results reported as the mean and standard deviation. For each experiment, a completely new iron/iron redox flow cell was assembled using new materials, including a membrane, copper plates, and electrodes. A newly prepared Fe^{2+} electrolyte solution was also employed before each test to mitigate oxidation-related issues and ensure consistency across all runs.

The IRFB single cell was cycled galvanostatically using the Gamry test system (Gamry Instruments, USA). For each test, 150 mL of electrolyte was used in each half cell, corresponding to a theoretical capacity of 6.10 A h (20.25 A h L^{-1}). The electrolyte flow rate was maintained at a constant 80 mL min^{-1} using a dual-line peristaltic pump. All operating conditions, including flow rate, electrolyte volumes, and cycling protocols, were kept identical across experiments conducted at 20 °C, 30 °C, 40 °C, and 50 °C to ensure a rigorous and fair comparison. The battery was charged and discharged at a constant current density of ±25 mA cm^{-2} (1 A total current) for a maximum duration of one hour per half-cycle, followed by a 5-minute rest period. An experiment consisted of 25 consecutive charge–discharge cycles. After completing an experimental series at a given temperature, the electrolyte was discarded, and the entire flow cell was disassembled and rebuilt with new components to eliminate potential carryover effects before initiating the next series. This protocol was consistently followed for all temperature experiments.

For long-term stability tests, a ''soft start'' protocol was employed. A new cell was assembled and first cycled for 10 cycles at 20 °C. Subsequently, the operating temperature increased to the target value of 40 °C, and cycling continued until performance degradation was observed. Throughout all experiments, upper and lower voltage limits of 1.9 V and 0 V, respectively, were set as safety cutoffs.

Results and discussion

Investigation of battery electrochemistry at varied temperatures

Cyclic voltammetry: insight into reaction kinetics. To investigate the electrochemical behavior of the system as a function of temperature, cyclic voltammetry (CV) was performed under stationary (non-flow) conditions to mitigate convective effects and ensure a diffusion-controlled environment. First, a background scan of the supporting electrolyte (2 M NH_4Cl and 0.2 M HCl) confirmed its electrochemical stability within the potential window of interest (−1.1 V to + 0.75 V *vs.* Ag/AgCl). As shown in Fig. 2(a), no significant Faradaic currents were observed, confirming that the supporting electrolyte is electrochemically inert and that subsequent observations can be attributed solely to the iron redox species.

The cyclic voltammograms of the complete 1.5 M Fe^{2+} electrolyte at various temperatures are presented in Fig. 2(b). The scans were initiated at 0 V *vs.* Ag/AgCl with a sweep toward positive potential. A distinct redox couple corresponding to the Fe^{2+}/Fe^{3+} reaction was observed, with an anodic peak around + 0.56 V *vs.* Ag/AgCl. For all temperatures, the peak separation (ΔE_p) was consistently greater than the theoretical 59 mV. This observation, combined with the fact that the ratio of anodic to cathodic peak currents (I_{pa}/I_{pc}) also deviated significantly from the ideal value of 1 (as detailed in Table 1), confirms the quasi-reversible nature of this reaction. A clear trend was observed: both the anodic and cathodic peak currents increased systematically with temperature, indicating enhanced mass transport. The data presented is from the second of three cycles, chosen to ensure a stable electrochemical response.

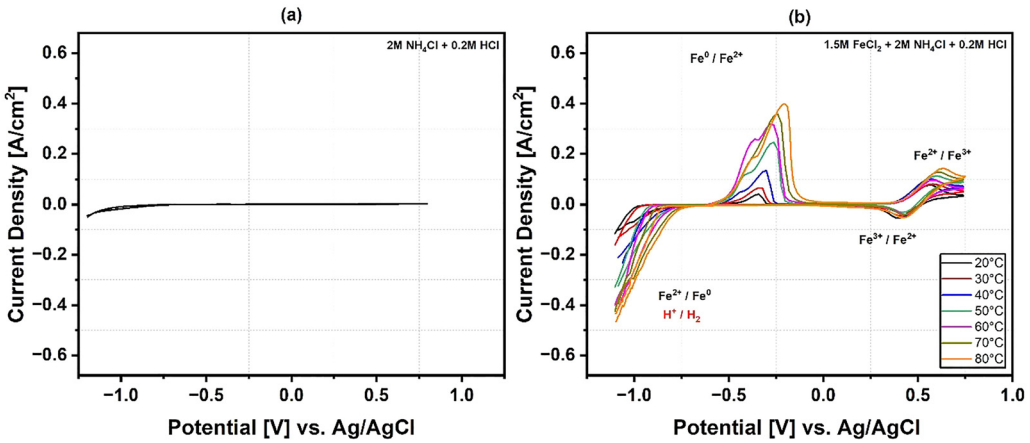

Fig. 2 (a) Electrochemical characterization of the electrolyte using a 3 mm diameter graphite working electrode, a platinum wire counter electrode, and an Ag/AgCl (3 M NaCl) reference electrode. (a) Cyclic voltammetry background scan of the supporting electrolyte (2 M NH_4Cl + 0.2 M HCl), confirming the electrochemical stability window at room temperature. (b) Cyclic voltammograms of the complete electrolyte (1.5 M $FeCl_2$ + 2 M NH_4Cl + 0.2 M HCl) at temperatures ranging from 20 °C to 80 °C (scan rate: 20 mV s^{-1}).

Table 1 Electrochemical kinetic parameters for the Fe^{2+}/Fe^{3+} redox couple at temperatures ranging from 20 °C to 80 °C. Data were obtained using a 3 mm diameter graphite working electrode, a Pt wire counter electrode, and an Ag/AgCl (3 M NaCl) reference electrode. The diffusion coefficients were calculated using the Randles–Sevcik equation

Temperature (°C)	Anodic peak current density (I_{pa}) (A cm^{-2})	Cathodic peak current density (I_{pc}) (A cm^{-2})	I_{pa}/I_{pc}	Anodic peak potential (E_{pa}) (V)	Cathodic potential (E_{pc}) (V)	Diffusion coefficient (cm^2 s^{-1})
20	0.071	0.06	1.19	0.562	0.399	1.89×10^{-6}
30	0.075	0.05	1.50	0.574	0.405	2.24×10^{-6}
40	0.094	0.08	1.18	0.564	0.43	3.75×10^{-6}
50	0.106	0.097	1.09	0.597	0.423	5.11×10^{-6}
60	0.112	0.098	1.14	0.58	0.439	5.56×10^{-6}
70	0.121	0.097	1.25	0.60883	0.428	7.15×10^{-6}
80	0.130	0.0784	1.66	0.62	0.438	8.93×10^{-6}

Upon reversing the scan toward negative potentials, a more pronounced shift is observed for the Fe^0/Fe^{2+} couple, beginning around −0.5 V *vs.* Ag/AgCl. As the temperature rises, the cathodic current becomes sharper and more intense, suggesting improved kinetics for metallic iron nucleation, plating, and hydrogen evolution. Nonetheless, the highly kinetically irreversible process remains evident. Critically, the onset of the parasitic hydrogen evolution reaction (HER) is also observed at more negative potentials (below −0.9 V). The sharp rise in cathodic current at 70 °C and 80 °C indicates that the kinetics of both the desired iron deposition and the unwanted HER are significantly enhanced. While improved plating kinetics are beneficial, the concurrent acceleration of HER introduces a critical trade-off, potentially lowering the battery's coulombic efficiency. This highlights the central challenge of managing performance gains against parasitic losses at elevated temperatures.

To quantify the effect of temperature on mass transport, the diffusion coefficient of the Fe^{2+} species was determined from CV's recorded at various scan rates (10–100 mV s^{-1}). As predicted by the Randles–Sevcik equation, the peak currents for the Fe^{2+}/Fe^{3+} couple scaled linearly with the square root of the scan rate. The strong linearity, confirmed by coefficients of determination (R^2) greater than 0.97 across all temperatures, provides definitive evidence that the reaction is predominantly diffusion-controlled. Based on this analysis, the calculated diffusion coefficient shows a nearly fivefold increase, from 1.89×10^{-6} cm^2 s^{-1} at 20 °C to 8.93×10^{-6} cm^2 s^{-1} at 80 °C. A systematic increase in both anodic and cathodic peak current densities with increasing scan rates is observed, indicative of a diffusion-controlled redox process at the electrode interface. The voltammograms exhibit consistent morphology without significant distortion, confirming the stability of the electrochemical reaction across the tested temperature range. However, a slight broadening of the peak potential separation at higher sweep rates suggests a quasi-reversible electron transfer mechanism for the Fe^{2+}/Fe^{3+} couple (Fig. 3).

It can be seen that there is a complete reversal of the trend in the battery's negative half-cell compared to the positive half-cell. Due to the presence of diffusion-controlled peaks observed on the positive side of the battery, the diffusion coefficient of Fe^{2+} ions was estimated exclusively from data on the positive half-cell.[39]

Fig. 4(a) illustrates that the Fe^{2+}/Fe^{3+} redox reaction is diffusion-controlled, as demonstrated by the linearity (R^2 value varying between 0.97 and 0.99) of the anodic peak current (I_{pa}) and cathodic peak current (I_{pc}) plotted against $\sqrt{}$scan rate. The accumulated data, with details, are tabulated below. The diffusion coefficient of Fe^{2+} in Fig. 4(b) was determined to be 1.89×10^{-6} cm^2 s^{-1} at 25 °C based on the slope of the linear fit and the assumption of a one-electron transfer (n = 1). At 80 °C of electrolyte temperature, the diffusion coefficient of Fe^{2+} was determined to be 8.93×10^{-6} cm^2 s^{-1}, nearly five times higher than at room temperature. The ratio of the peak currents was observed to be near 1, suggesting a nearly reversible relationship in Fe^{2+}/Fe^{3+} redox reactions. The figure above shows the influence of temperature on diffusion coefficients.

There was a proportional correlation between temperature and the diffusion coefficient, as shown in Fig. 4(b), suggesting that ionic mobility increased at higher temperatures. This temperature dependence of the diffusion coefficient indicates improved charge transport and redox kinetics in the positive half-cell at elevated temperatures, thereby validating the observed rise in peak current with increasing temperature. Furthermore, the temperature influence is reflected in the kinetic onset potential; as temperature increases, a shift toward lower overpotentials is observed, indicating a reduction in the activation energy barrier for the Fe^{2+}/Fe^{3+} redox reaction. This enhancement in both mass transport and electron-transfer kinetics validates the significant increase in peak current densities observed at higher temperatures.

Influence of temperature on iron deposition morphology

The morphology of the electrodeposited iron is critical to the long-term stability and performance of the negative electrode. To investigate this, iron was deposited potentiostatically at −1.2 V *vs.* Ag/AgCl (3 M NaCl) for 120 s onto a graphite disk electrode at temperatures ranging from 20 °C to 50 °C. This method provides a constant electrochemical driving force, allowing for a direct comparison of the resulting film structures.

The optical microscopy images in Fig. 5 reveal a clear evolution in deposit morphology with increasing temperature. At 20 °C, the deposit is relatively uniform and dense, exhibiting a microcrystalline structure consistent with slower nucleation kinetics and limited surface diffusion of iron adatoms. As the

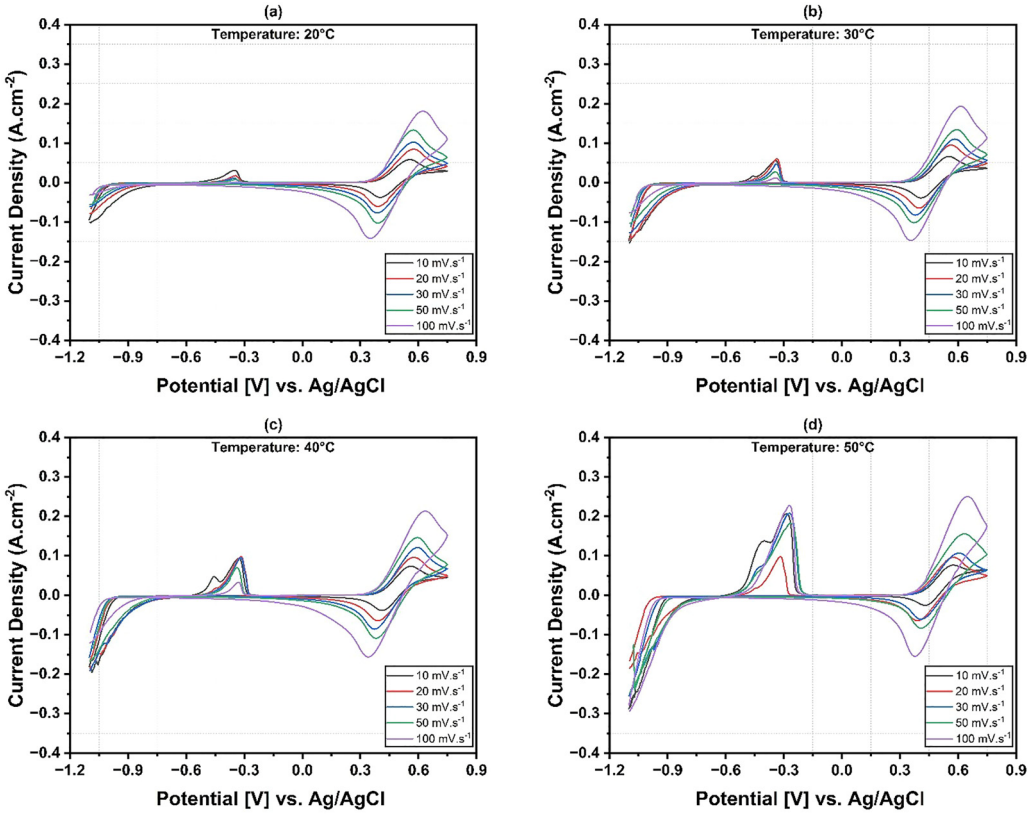

Fig. 3 Cyclic voltammograms of the electrolyte recorded at scan rates ranging from 10 to 100 mV s^{-1} at operating temperatures of (a) 20 °C, (b) 30 °C, (c) 40 °C, and (d) 50 °C. Measurements were performed using a 3 mm diameter graphite working electrode, a platinum wire counter electrode, and an Ag/AgCl (3 M NaCl) reference electrode.

temperature rises to 30 °C and 40 °C, the deposit transitions to a structure with significantly larger and more defined crystalline domains. This change is attributed to increased adatom mobility, which allows atoms to diffuse across the surface and organize into lower-energy crystalline sites. However, this enhanced kinetic freedom is accompanied by the formation of significant cracks and fissures. These defects likely arise from a combination of internal stresses caused by lattice mismatch and hydrogen incorporation and the disruptive effect of co-evolving hydrogen, which can create high-pressure voids and lead to embrittlement. At 50 °C, these detrimental effects dominate, resulting in large, poorly adhered plate-like structures that show clear signs of delamination from the substrate. These qualitative observations are corroborated by quantitative

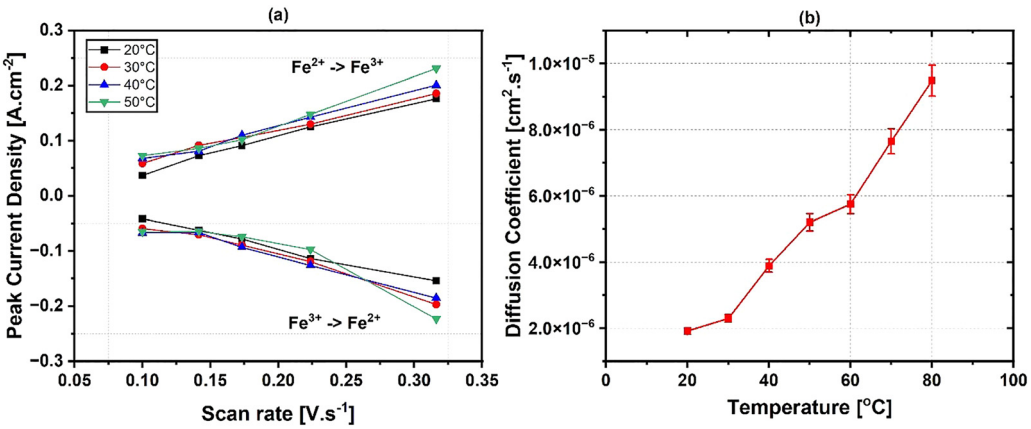

Fig. 4 Kinetic parameter determination. (a) Randles–Sevcik plots of anodic (Fe^{2+}/Fe^{3+}) and cathodic (Fe^{3+}/Fe^{2+}) peak current densities *versus* the square root of the scan rate, confirming diffusion-controlled behavior. (b) Calculated diffusion coefficient of the Fe^{2+} species as a function of temperature, demonstrating a fivefold increase from 20 °C to 80 °C.

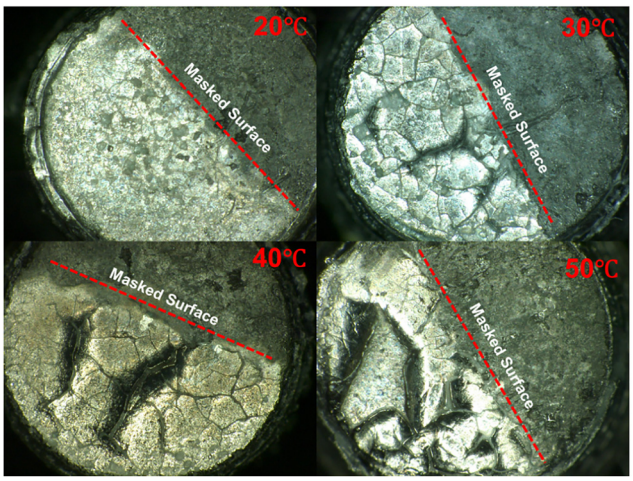

Fig. 5 Morphological evolution of iron deposits. Optical microscopy images of iron films deposited potentiostatically (−1.2 V *vs.* Ag/AgCl (3 M NaCl) for 120 s) on a graphite substrate at varied temperatures.

analysis from confocal microscopy (Fig. 6(a)). The 3D profiles confirm the trend of increasing surface roughness and highlight the deep fissures that develop at higher temperatures. The average thickness of the deposited iron, plotted in Fig. 6b, increases from 15 μm at 20 °C to a maximum of 41 μm at 40 °C, which is consistent with the thermally enhanced deposition kinetics. Strikingly, the average thickness then decreases to 37 μm at 50 °C. This reduction, despite the highest kinetic rate, is direct evidence of poor mechanical integrity; the delamination and flaking of large deposit sections, as seen in Fig. 5, leads to a lower average thickness measured across the electrode surface.

At elevated temperatures, the hydrogen evolution reaction (HER) intensifies at the electrode–electrolyte interface. The rapid formation and release of hydrogen bubbles within the growing metal layer result in localized voids and micro-cracks. These trapped gas pockets disrupt uniform nucleation, weaken adhesion between the metal and the substrate, and introduce tensile stresses during bubble detachment. Additionally, as the co-evolved hydrogen diffuses through the deposit, it can lead to embrittlement and partial lifting of the plated iron, elucidating the porous and discontinuous morphology observed at 50 °C. Therefore, the interaction between accelerated iron deposition and heightened hydrogen evolution explains both the increased apparent growth rate and the significant structural degradation at elevated temperatures.

Ultimately, these results reveal a critical trade-off: while elevated temperatures accelerate the iron deposition rate, it has simultaneously compromised the deposit's structural integrity, but no dendrites were seen. This can lead to severe operational issues such as active material loss and rapid capacity fading, posing a significant challenge to achieving stable, long-term battery cycling. These experimental observations are consistent with fundamental electrochemical principles, which state that elevated temperatures exponentially increase the reaction rate constant for both metal deposition and the parasitic hydrogen evolution reaction. Prior studies on iron-based electrolytes have demonstrated that although elevated temperatures increase the absolute rate of hydrogen evolution reaction (HER), they also significantly modify iron plating kinetics. This underscores the importance of actively managing thermal conditions.[40]

Linear sweep voltammetry analysis of iron plating and stripping behavior

To quantitatively assess the competition between iron deposition and the parasitic HER, the coulombic efficiency of the

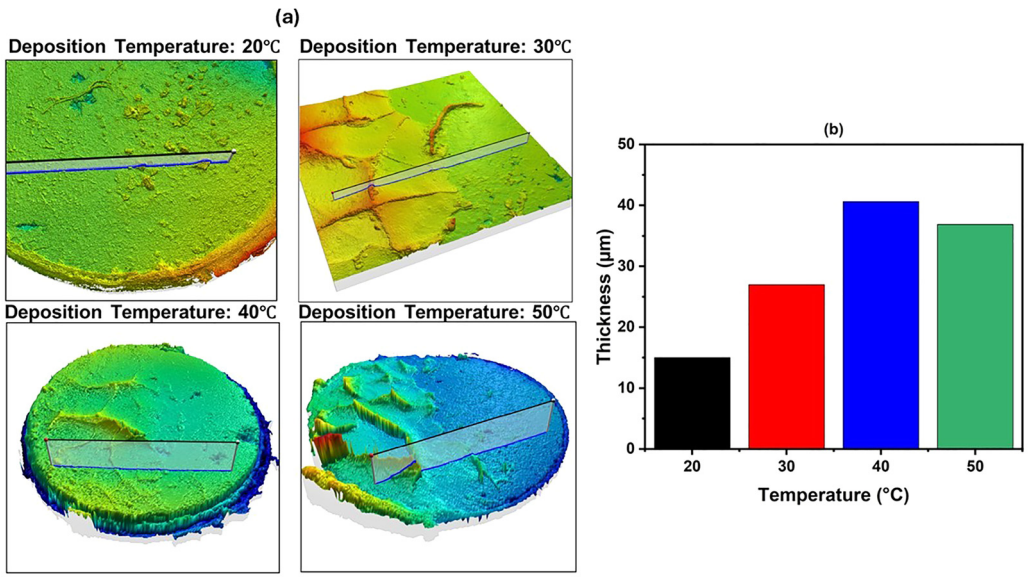

Fig. 6 Topographical analysis. (a) Confocal laser scanning microscopy (CLSM) 3D surface profiles of the iron layers potentiostatically deposited at −1.2 V *vs.* Ag/AgCl (3 M NaCl) for 120 s onto a graphite disk electrode. (b) Quantitative analysis of deposit thickness *versus* temperature, highlighting the impact of rapid growth kinetics and delamination at various temperatures.

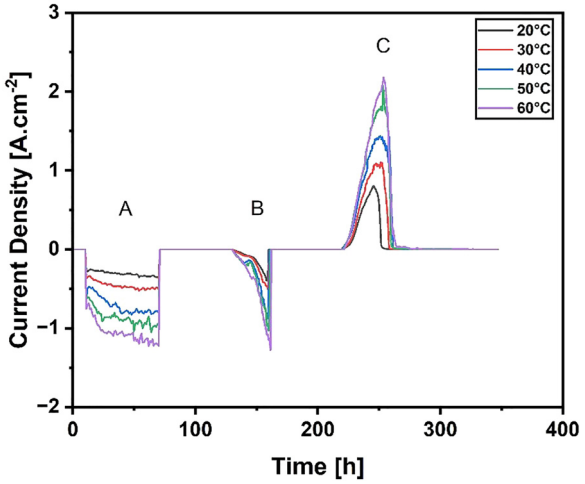

Fig. 7 Chronological current density response for the iron plating/stripping protocol. The measurement was performed using a 3 mm graphite working electrode, a Pt wire counter electrode, and an Ag/AgCl (3 M NaCl) reference electrode. (A) Potentiostatic iron deposition at − 1.2 V *vs.* Ag/AgCl for 60 s. (B) Cathodic linear sweep from OCP to −1.2 V *vs.* Ag/AgCl (at 20 mV s^{-1}) to complete the plating process. (C) Anodic linear sweep from OCP to + 0.2 V *vs.* Ag/AgCl (at 20 mV s^{-1}) to strip the deposited iron. Data are shown for temperatures ranging from 20 °C to 60 °C.

plating/stripping process was determined using linear sweep voltammetry (LSV). This technique was chosen as it allows for the independent management of the deposition and dissolution processes, enabling a more precise quantification of each half-reaction than cyclic voltammetry, as first demonstrated by Hilbert in 1971 for metal deposition systems.[41] The experimental protocol was designed to provide a practical insight into how the plating efficiency varies with temperature. As the exchange-current density for HER differs significantly on a bare graphite surface *versus* a freshly plated iron surface, a two-step deposition process was employed to create a more representative substrate. First, a potentiostatic hold at −1.2 V *vs.* Ag/AgCl (3 M NaCl) for 60 s established an initial iron layer (Fig. 7a, region A), followed by a cathodic linear sweep from OCV to −1.2 V *vs.* Ag/AgCl (3 M NaCl) to complete the deposition (Fig. 7a, region B), following the methodology previously reported by Noack *et al.* for iron electrolyte characterization in IRFB systems.[42] Subsequently, an anodic sweep from OCV to + 0.2 V was performed to strip the deposited iron (Fig. 7, region C), and the corresponding anodic charge (Q_{strip}) was integrated.

From the figure above, it can be stated that as temperature increases, the kinetics of the redox reaction at the negative half-cell side of the battery improve. The individual voltammograms in Fig. 9(a)–(c) clearly show that the current densities for both deposition and stripping increase with temperature, confirming the enhanced kinetics observed in the CV analysis. However, the calculated coulombic efficiency (CE), defined as CE = $(Q_{strip}/Q_{dep}) \times 100\%$, reveals a more complex, non-monotonic relationship with temperature, as shown in Fig. 9(d). The CE increases from approximately 58% at 20 °C to a distinct maximum of ∼71% at 30 °C. This initial improvement suggests that in this temperature range, the activation energy for iron deposition is reduced more significantly than that for HER, making the desired plating reaction kinetically more favorable. Beyond this peak, as the temperature increases to 40 °C, 50 °C, and 60 °C, the CE progressively decreases, falling to ∼59% at 60 °C. This reversal indicates that at higher temperatures ($T > 30$ °C), the acceleration of the HER becomes the dominant kinetic effect. A larger fraction of the charge is consumed by this parasitic reaction, resulting in a net loss of plating efficiency. This finding is critical, as it demonstrates a clear kinetic trade-off and predicts an optimal operating temperature for the full cell, where the detrimental effects of excessive hydrogen evolution do not yet outweigh the benefits of enhanced iron kinetics. Additionally, as shown in Fig. 8, a gradual change in the electrolyte color from its initial light green to a more yellowish hue was observed at higher temperatures, suggesting some degree of aerial oxidation of Fe^{2+} to Fe^{3+}, which could be a key contributor to efficiency loss.

Thus, the effect of temperature was significant on redox kinetics, deposition morphology, and coulombic efficiency of metal deposition and stripping when studied in an electrochemical bath. There was a clear indication of improved diffusion of Fe^{2+} and an indication of better ionic mobility in the positive half-cell side of the battery at higher temperatures. However, the kinetically irreversible negative half-cell side electrochemical reactions were more complex to study because of the involvement of the parasitic hydrogen evolution reaction.

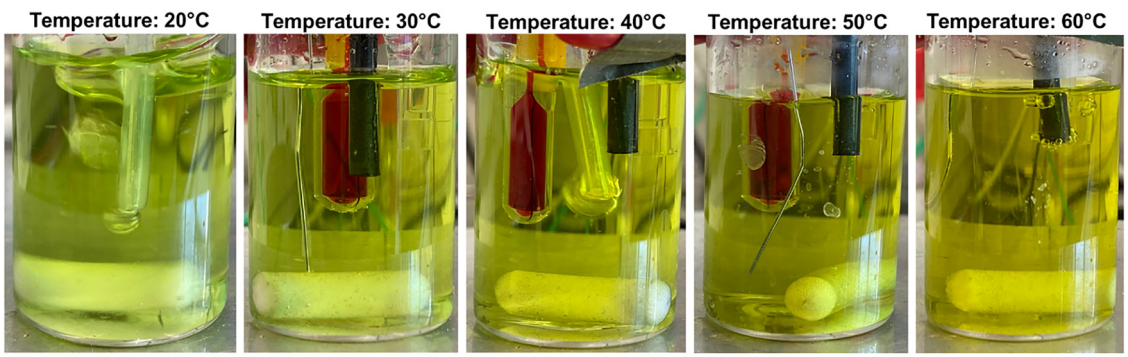

Fig. 8 Visual comparison of electrolyte samples after exposure to temperatures from 20 °C to 60 °C, with indication of H2 bubbles at higher temperatures.

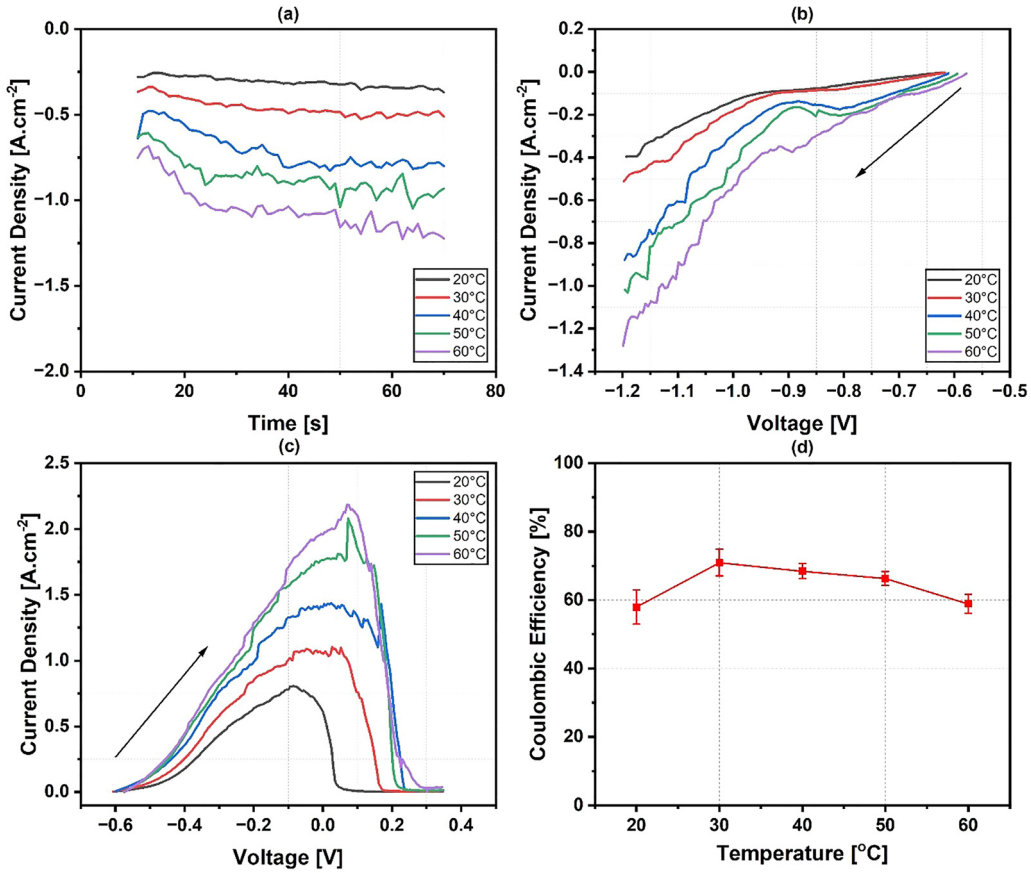

Fig. 9 Effect of temperature on (a) potentiostatic iron deposition, (b) sweeping potential deposition, (c) stripping, (d) Coulombic efficiency of iron plating and stripping process.

Overall, the electroanalytical tests provided an indicative picture of what to expect in practical battery operation. Problems such as electrolyte oxidation, capacity loss, and excessive hydrogen evolution might inhibit battery performance. However, improved diffusion and reaction kinetics might counteract these effects, as discussed later in this section.

Influence of operating temperature on cycling performance

Following the fundamental electrochemical characterization, the performance of a complete 40 cm^2 lab-scale IRFB cell was evaluated under galvanostatic cycling conditions to understand the integrated effects of temperature on practical operation. The experiments investigated the battery's performance at operating temperatures of 20 °C, 30 °C, 40 °C, and 50 °C. For each temperature, a new cell was assembled and filled with 150 mL of electrolyte per side, corresponding to a theoretical capacity of 6.10 A h (20.25 A h L^{-1}). The battery was cycled at a constant current density of ±25 mA cm^{-2} for a 1-hour charge and a maximum of 1 hour of discharge, representing a theoretical capacity utilization of ~17% per cycle. To ensure statistical robustness, each temperature experiment was conducted twice, and the results are presented as mean values with standard deviations. All results presented were obtained using an optimized system incorporating an active hydrogen management loop. The charge and discharge voltage curves recorded for each experiment were utilized to calculate the respective capacities and efficiencies.

The discharge capacity, shown in Fig. 10(a), exhibited a clear positive correlation with operating temperature during the initial cycling phase. At 20 °C, the battery delivered an initial discharge capacity of approximately 0.55 A h. As the temperature increased, the discharge capacity systematically increased, reflecting reduced overpotentials and enhanced diffusion kinetics of the Fe^{2+} species identified in the half-cell studies. Notably, the cell operating at 40 °C exhibited superior capacity retention, steadily rising to approximately 0.85 A h by the 25th cycle. However, the stability limit was reached at 50 °C. While this temperature initially supported the highest capacities due to maximized kinetics, performance became erratic in later cycles, consistent with the physical degradation observed in the morphological study.

The coulombic efficiency (CE) trends, shown in Fig. 10(b), reveal the complex interplay between iron deposition and the parasitic hydrogen evolution reaction (HER). In the first cycle, the coulombic efficiencies were recorded as 55.43% at room temperature, 52.69% at 30 °C, 54.15% at 40 °C, and 48.78% at 50 °C. It was observed that lower coulombic efficiencies are typically seen during the initial startup cycles at higher

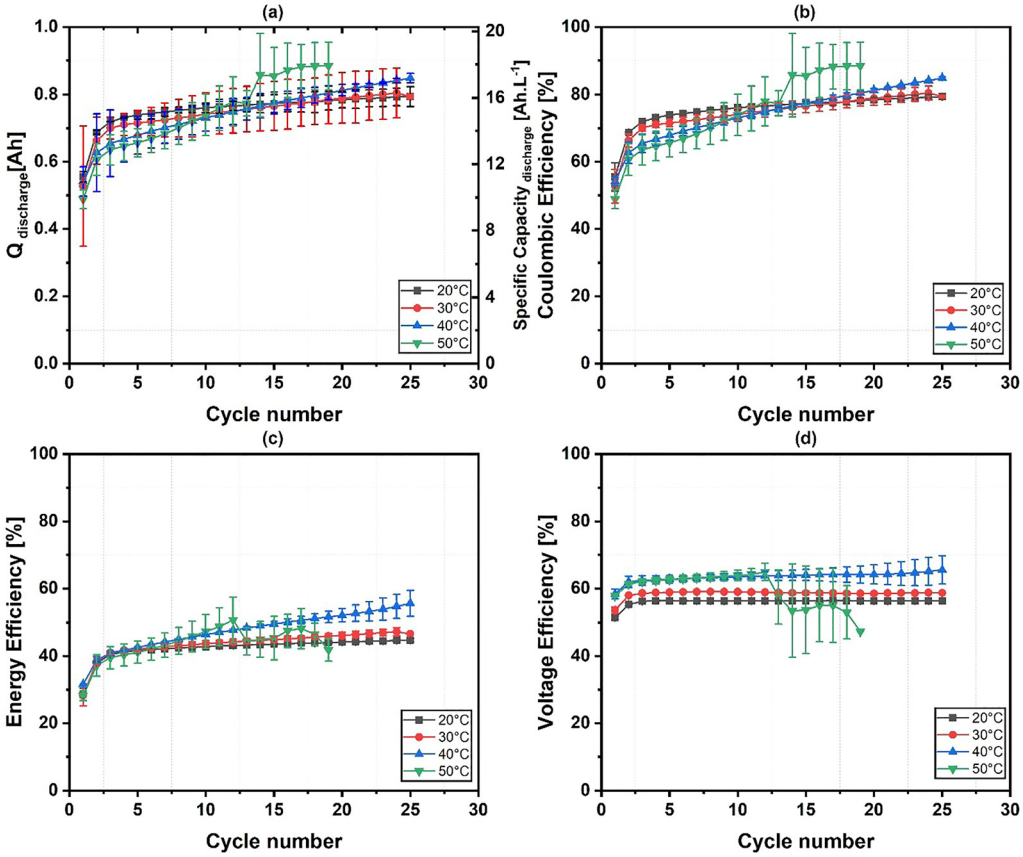

Fig. 10 Performance metrics of IRFBs at different operating temperatures with a constant 1-hour charge/discharge. (a) discharge capacity/specific discharge capacity *vs.* cycles, (b) coulombic efficiency *vs.* cycles, (c) energy efficiency *vs.* cycles, (d) voltage efficiency *vs.* cycles. The experiments were conducted at various operating temperatures, yielding a theoretical capacity of 6.10 A h (20.25 A h L^{-1}). The electrolyte composition was 1.5 M $FeCl_2$, 2 M NH_4Cl, and 0.2 M HCl. The charge/discharge process employed a 5-minute rest period and a current density of 25 mA cm^{-2}. All experiments are the mean of two experiments with standard deviations.

operating temperatures. This behavior can be attributed to the battery's unsteady-state conditions during early cycling. The primary reason for the decrease in coulombic efficiency, as indicated by linear sweep voltammetry (LSV) results, is the evolution of hydrogen. At elevated temperatures, the hydrogen evolution reaction is believed to be exacerbated, leading to lower coulombic efficiencies. However, with the implementation of the hydrogen recycling technique (refer to the experimental setup section), the hydrogen recombination efficiency improved. This improvement helps maintain a relatively stable pH level, supporting the understanding that the initial drop in coulombic efficiency is related to the kinetics of hydrogen evolution. In Fig. 11(a) and (b), at an operating temperature of 30 °C and without hydrogen recycling, the recombination cell current was below 100 mA due to an inconsistent hydrogen purge. However, with hydrogen recycling, the current increased dramatically to 360 mA in the first cycle and remained consistently above 200 mA over 25 cycles. A trend reversal in the coulombic efficiency curve was noted after the tenth cycle. At higher operating temperatures, the coulombic efficiency improves with each cycle, indicating better hydrogen back diffusion, a more stable system, and comparatively less charge loss due to hydrogen evolution.

In contrast, voltage efficiency exhibited the expected trend of increasing with temperature. This improvement can likely be attributed to enhanced ionic conduction through current collectors, better ionic mobility, and reduced internal resistance at higher temperatures. After the 25th cycle, a maximum voltage efficiency of 66% was recorded at an operating temperature of 40 °C, followed by efficiencies of 58.7% at 30 °C and 56.3% at room temperature. The lowest voltage efficiency was observed at 50 °C, where heavy precipitation led to significant ohmic resistance in the battery. Following the 25th cycle, the highest energy efficiency, nearly 56%, was achieved at 40 °C. In comparison, the energy efficiencies at room temperature and 30 °C were 44% and 47%, respectively. The improvements in voltaic and coulombic efficiencies after the 25th cycle contributed to a 10% increase in overall energy efficiency. For optimal battery performance and to ensure 90% precipitation-free operation, 40 °C was identified as the ideal operating temperature for future tests. It should be noted that, due to hydrogen recycling, the constant pH-maintaining technique has shown slightly

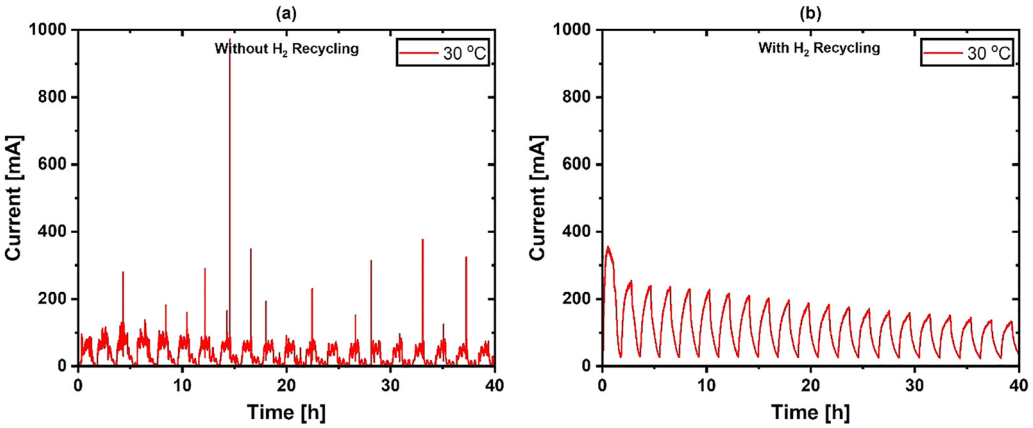

Fig. 11 Impact of hydrogen recycling technique on the recombination cell current in an IRFB (a) recombination cell current profile over time without H_2 recycling, (b) recombination current profile over time with H_2 recycling. The experiments were conducted at various operating temperatures, yielding a theoretical capacity of 6.10 A h (20.25 A h L^{-1}). The electrolyte composition was 1.5 M $FeCl_2$, 2 M NH_4Cl, and 0.2 M HCl. The charge/discharge process lasted a maximum of 1 hour, with a 5-minute rest period at a current density of 25 mA cm^{-2}.

lower efficiencies and requires more cycles to reach higher efficiencies, indicating an alkaline state, as shown in Fig. 13.

Effect of battery operating temperature on HER and hydrogen recombination

The operating temperature of the flow battery system significantly influences the rate of the parasitic hydrogen evolution reaction (HER) at the negative electrode, which dictates the volume of H_2 gas directed to the recombination cell. Fig. 12 illustrates the current signal from the recombination cell at varied temperatures. The data demonstrates a clear increase in recombination capacity at elevated temperatures. This enhanced capacity is a direct result of two compounding factors: the accelerated HER kinetics in the main battery, which provides a higher partial pressure of H_2 reactant, and the improved catalytic reaction kinetics for hydrogen oxidation and Fe^{3+} reduction within the recombination cell itself due to the added thermal energy. To quantify the efficacy of the hydrogen management system, the recombined capacity (Q_{rec}) was calculated by integrating the instantaneous current (I_{rec}) measured at the recombination cell over the cycling period. This value represents the total charge recovered *via* the electrochemical oxidation of hydrogen and serves as a direct metric of the volume of gas successfully redissolved into the electrolyte. By comparing this recombined capacity against the theoretical capacity loss, the recombination efficiency was derived for each thermal condition.

In the study, 25 cycles were conducted at four different temperatures (20 °C, 30 °C, 40 °C, and 50 °C) to measure capacity loss, the amount of recombined hydrogen (in mAh), and recombination efficiency. The recombination efficiency remained relatively constant at approximately 25% at 20 °C across all cycles. This consistency suggests that slow and stable rates of hydrogen recombination are likely due to slow reaction kinetics and low conversion rates from hydrogen (H_2) to protons (H^+).[43] At 30 °C, recombination efficiency gradually decreased from 24.1% to 21.1% by the 25th cycle (see Table 2). This decline may indicate a slow loss of unconverted

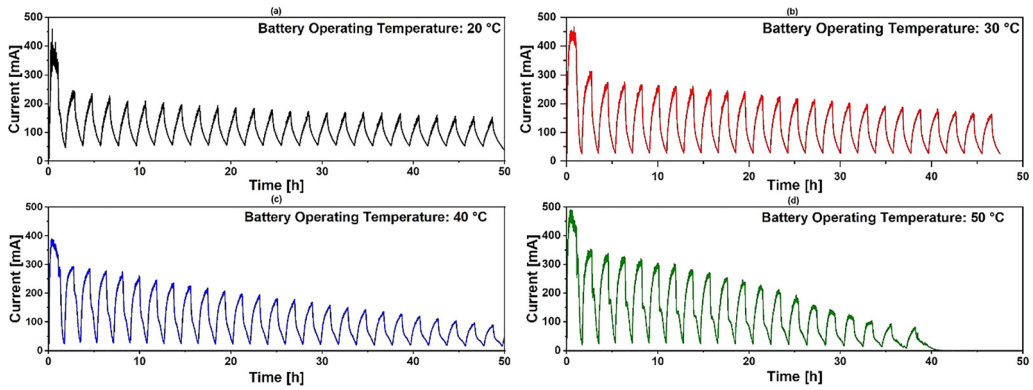

Fig. 12 Recombination cell current signal at different battery operating temperatures with a maximum 1-hour charge/discharge process of IRFB for 25 cycles. The experiments were conducted at different battery operating temperatures with a theoretical capacity of 6.10 A h (20.25 A h L^{-1}). The electrolyte composition was 1.5 M $FeCl_2$, 2 M NH_4Cl, and 0.2 M HCl. The charge/discharge process employed a 5-minute rest period and a current density of 25 mA cm^{-2}.

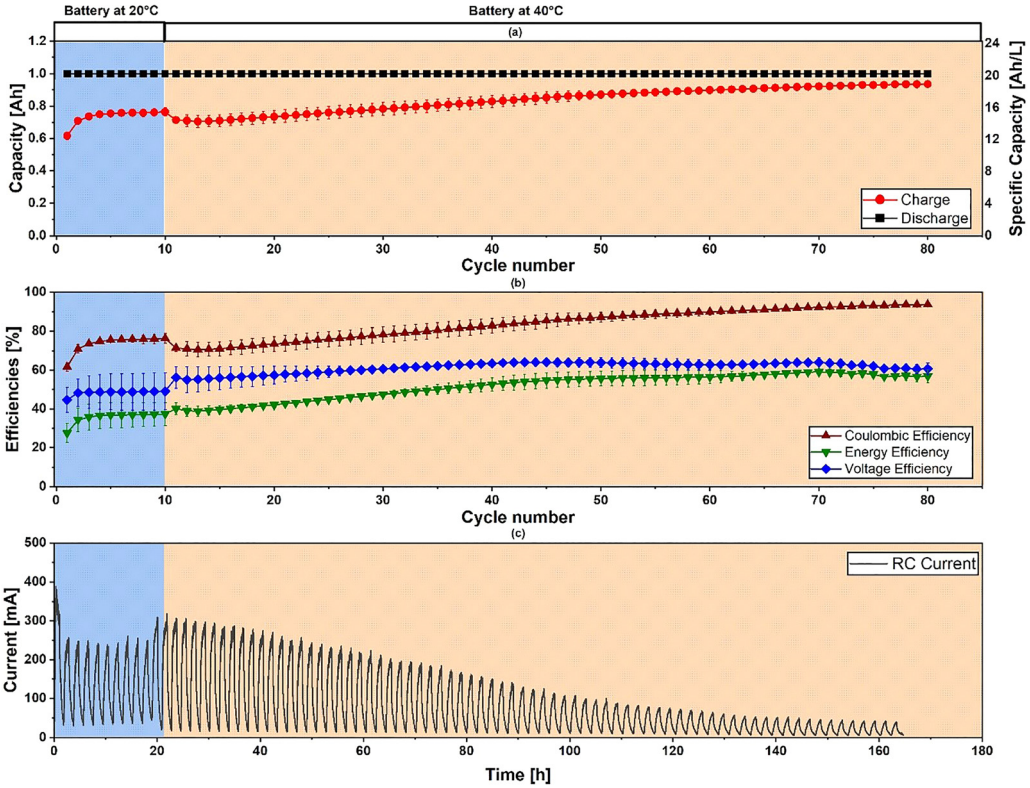

Fig. 13 Performance metrics of the recombination cell and battery with a 'soft start' testing protocol. (a) Charge/discharge capacity and specific capacity *vs.* cycle number. (b) Coulombic, energy, and voltage efficiencies *vs.* cycle number. (c) The recombination cell current profile over time. The experiments were conducted at various operating temperatures, yielding a theoretical capacity of 6.10 A h (20.25 A h L^{-1}). The electrolyte composition was 1.5 M $FeCl_2$, 2 M NH_4Cl, and 0.2 M HCl. The charge/discharge process of a maximum of 1 hour was employed with a rest period of 5 minutes and a current density of 25 mA cm^{-2}.

hydrogen due to a small system leak or insufficient pressure control. At 40 °C, the recombination efficiency was relatively higher at 26.9% but fell to about 20.6% by the 25th cycle. Although higher temperatures initially promote faster recombination, prolonged cycling may reduce the availability of H_2 due to increased coulombic efficiency in the iron/iron flow cell, slight positive shifts in pH due to electrolyte imbalance, or potential gas loss from the system. At 50 °C, an initial increase in recombination efficiency was observed, reaching up to 38.3% by cycle 20. However, this apparent improvement is misleading, as heavy precipitation began to develop within the system, potentially shifting pH toward more positive values and ultimately leading to system failure around cycle 15.

As shown in Fig. 12, a sharp current peak is observed at the start of discharge. The exact cause of this peak is uncertain. Still, two primary factors could be contributing: the utilization of unused hydrogen from the back-pressure tank, and the chemical corrosion of the freshly electrodeposited iron (Fe^0) driven by the low pH of the electrolyte. Considering the improved kinetics without precipitation-related issues, the optimal operating window for efficient hydrogen recombination appears to be between 30 °C and 40 °C. Although 50 °C has the highest numerical recombination efficiency ratings, it is not a stable or sustainable operating temperature, as indicated by the onset of precipitation and membrane fouling. Effective hydrogen recycling, improved tank sealing, and system volume optimization are crucial, but only within a thermally stable range. These findings highlight the critical role of temperature in determining the effectiveness of hydrogen recombination and the system's overall stability. Higher temperatures can enhance hydrogen recombination and reaction kinetics but also present significant challenges, such as precipitation and membrane fouling.

Ultimately, a balanced approach to recombination performance, based on current findings, suggests that an ideal working temperature is around 40 °C. However, without data on hydrogen generation and hydrogen back-diffusion to the negative side of the cell, the full picture of hydrogen utilization remains unclear. Although measuring the recombination cell current provides an estimate of hydrogen generation, direct quantification remains necessary. For instance, previous studies have investigated the spatial distribution of evolved hydrogen gas and local pH effects during iron plating using operando neutron imaging.[43] Another study employed in-line gas chromatography during battery cycling, with hydrogen gas collected simultaneously in an inverted water-filled graduated cylinder.[44] Expanding on these diagnostic capabilities, recent advancements have utilized operando synchrotron X-

Table 2 Key performance metrics for hydrogen recombination at various operating temperatures (20–50 °C) over 25 cycles. The experiments were conducted at various operating temperatures, yielding a theoretical capacity of 6.10 A h (20.25 A h L^{-1}). The electrolyte composition was 1.5 M $FeCl_2$, 2 M NH_4Cl, and 0.2 M HCl. The charge/discharge process lasted up to 1 hour, with a 5-minute rest period at a current density of 25 mA cm^{-2}

Temperature (°C)	Cycle number	Coulombic efficiency (%)	Unrecovered capacity (mAh)	Capacity recombined (mAh)	Recombination efficiency (%)
20	1	55.44	1604.2	402.61	25.10
	5	73.89	940.0	236.9	25.20
	10	76	864.0	219.32	25.38
	15	77.29	817.6	204.8	25.05
	20	78.4	777.6	195.42	25.13
	25	79.33	744.1	184.64	24.81
30	1	52.69	1703.2	390	22.90
	5	71.5	1026.0	247.2	24.09
	10	74.1	932.4	216.6	23.23
	15	76.5	846.0	190	22.46
	20	78.87	760.7	181.7	23.89
	25	79.36	743.0	156.7	21.09
40	1	54.11	1652.0	445	26.94
	5	67.8	1159.2	290.49	25.06
	10	73.07	969.5	238.95	24.65
	15	77.4	813.6	193.72	23.81
	20	81.2	676.8	151.31	22.36
	25	84.7	550.8	113.37	20.58
50	1	48.75	1845.0	543.24	29.44
	5	65.57	1239.5	357.2	28.82
	10	73.9	939.6	283.2	30.14
	15	85.4	525.6	182.96	34.81
	20	93.4	237.6	91	38.30

ray microtomography, combined with deep learning-based image segmentation, to quantify and spatially resolve the three-dimensional distribution of trapped hydrogen bubbles within thick, porous electrodes in vanadium redox flow batteries.[45] Additionally, analytical tools such as the electrochemical quartz crystal microbalance (EQCM) have demonstrated high effectiveness in directly distinguishing real-time metal electrodeposition rates from competing parasitic hydrogen evolution reaction (HER) currents in low-pH environments in aqueous zinc metal batteries.[46] Incorporating these advanced operando diagnostic techniques into thermally modulated iron redox flow battery (IRFB) systems constitutes a critical direction for future research. By mapping localized gas evolution and separating competing reaction kinetics, future studies can determine the precise parameters required to optimize active hydrogen recombination systems for long-duration energy storage. Although future research will require these advanced operando tools, the hydrogen recombination and pH tracking used in this study establish the fundamental thermal and operational limits required to stabilize these complex, gas-producing systems.

The next sections will present results from longer cycling experiments using these optimized conditions as a baseline to evaluate system robustness, efficiency retention, and long-term durability under real-world operating conditions.

Soft-start temperature strategy for enhanced long-term cycling performance

The long-term stability of the iron-based redox flow battery (IRFB) was comprehensively assessed through extended galvanostatic cycling at elevated temperatures, utilizing an electrolyte volume of 150 : 150 mL in both the negative and positive reservoirs. This configuration corresponds to a theoretical capacity of 6.10 A h, equivalent to 20.25 A h L^{-1}, thereby establishing an upper limit for accessible charge storage. The cycling protocol involved a one-hour charging step followed by a maximum one-hour discharge step, incorporating a 5-minute rest interval between charge and discharge to facilitate system equilibration. These parameters were specifically selected to minimize transient effects and ensure that efficiency metrics accurately reflected the cell's intrinsic electrochemical performance.

To evaluate the long-term stability of the system under the previously identified optimal conditions, extended cycling tests were conducted at 40 °C. Initial findings indicated that continuous operation at this temperature from the outset resulted in performance degradation after approximately 40 stable cycles, eventually leading to failure due to precipitation and pH imbalance. It was hypothesized that the high rate of hydrogen evolution during the initial, most critical phase of cycling at 40 °C induced an electrolyte imbalance that the rebalancing system could not sufficiently rectify over time.

To overcome this limitation, a "soft-start" protocol was implemented. This protocol involved conditioning the battery at room temperature (20 °C) for the first 10 cycles before increasing the temperature to the optimal 40 °C. This approach leverages the higher initial coulombic efficiency at lower temperatures to minimize hydrogen loss during the critical system start-up phase. The results of this strategy, shown in Fig. 13(a), demonstrate a remarkable improvement in durability. The

battery operated stably for over 140 hours and completed more than 75 cycles before the electrolyte became turbid. This represents a twofold increase in the operational lifetime compared to the standard high-temperature start. The efficiency trends during the soft-start test followed the anticipated pattern. During the initial 10 cycles at 20 °C, the efficiencies and recombination current (see Fig. 13(b)) remained stable. Upon switching to 40 °C, a transient drop in coulombic efficiency was observed, corresponding to an increased rate of hydrogen evolution, as validated by an immediate increase in the recombination current. Concurrently, a significant increase in voltaic efficiency was observed due to the improved ionic mobility and electronic conductivity at the higher temperature. As cycling continued at 40 °C, the coulombic efficiency steadily recovered, reaching a maximum of 94% by the 80th cycle, with corresponding energy and voltaic efficiencies of 60% and 63%, respectively. Here, the hydrogen recycling technique also helped for better recombining efficiency at higher temperatures. This demonstrates that the soft-start protocol is a highly effective strategy for enhancing the long-term stability and performance of the IRFB system at higher temperatures.

Extended soft-start validation under high-capacity CCCV operation with *in situ* pH monitoring

To extend and validate the ''soft-start'' strategy outlined in the previous section, a supplementary investigation was carried out under conditions of high-capacity utilization. Unlike the time-limited galvanostatic cycling (with a 1-hour cutoff) used in the earlier stability tests, this study employed a constant current constant voltage (CCCV) protocol. This approach allows the battery to fully access its theoretical capacity, thereby subjecting the electrolyte and the electrode interface to maximum stress due to pH shifts and the kinetics of parasitic reactions. The experiment utilized a scaled-up electrolyte volume of 400 mL per reservoir, equating to a theoretical capacity of 16.08 A h (20.25 A h L^{-1}). The cell was cycled with cutoff limits of 1.9 V for charging and 0 V for discharging, and a current cutoff of 100 mA. As shown in Fig. 14, the cell underwent an initial conditioning phase at 20 °C (cycles 1–3) before the thermal management system implemented a step change to the optimal operating temperature of 40 °C (cycles 4–15).

The electrochemical performance analysis presented in Fig. 14 reveals a marked distinction in system behavior between the initial conditioning phase and subsequent high-temperature operation. Panel (a) illustrates capacity evolution, in which the initial cycles at 20 °C show a notable disparity between charge and discharge capacities. Specifically, the charge capacity in the first cycle increases to approximately 21.5 A h, significantly surpassing the theoretical capacity limit of 16.08 A h set by the electrolyte volume. This phenomenon of overcharge suggests a predominant hydrogen evolution reaction (HER), indicating that a substantial portion of the applied current is directed towards the reduction of protons rather than the reduction of ferrous ions (Fe^{2+}). Consequently, the discharge capacity remains limited to around 14 A h, resulting in a considerably reduced Coulombic efficiency (CE) of roughly 63%, as shown in panel (b). This inefficiency during the startup phase is a calculated trade-off associated with the soft-start protocol; operating at 20 °C mitigates the rate of precipitate formation, thereby allowing a coherent initial iron layer to nucleate on the carbon felt substrate, despite the occurrence of hydrogen evolution.

Upon transitioning to 40 °C at cycle 4, the system enters a critical thermal equilibration phase. As expected, the

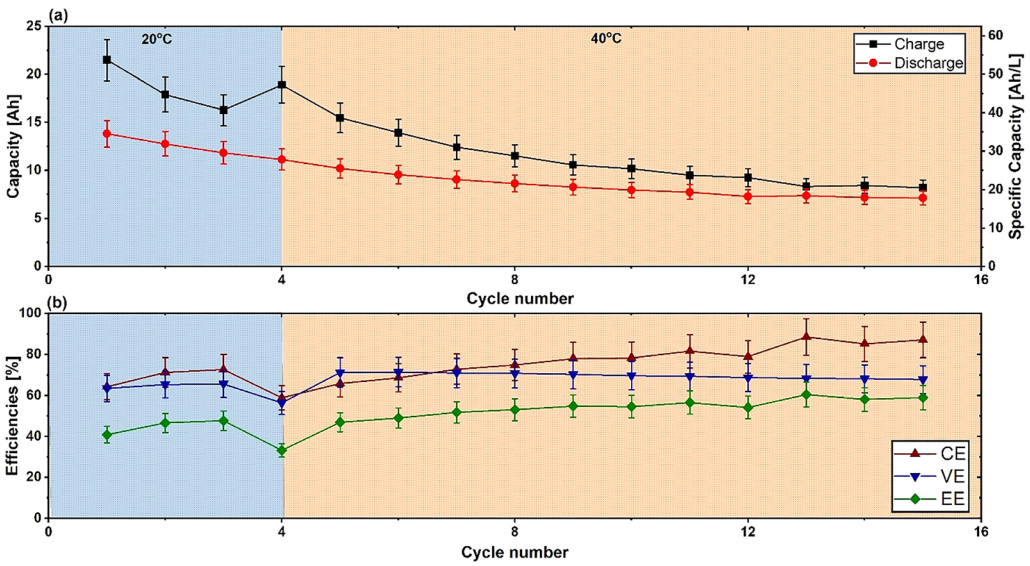

Fig. 14 Extended soft-start validation under high-capacity utilization. (a) Evolution of charge/discharge capacity and specific capacity as a function of cycle number. (b) Coulombic, energy, and voltage efficiencies *vs.* cycle number. The experiments employed a constant current constant voltage (CCCV) protocol with voltage limits of 1.9 V (charge) and 0 V (discharge) and a cutoff current of 100 mA. A scaled-up electrolyte volume of 400 mL per reservoir was used, corresponding to a theoretical capacity of 16.08 A h (20.25 A h L^{-1}). The system was conditioned at 20 °C (blue-shaded region) before transitioning to 40 °C (orange-shaded region).

immediate application of thermal energy accelerates the kinetics of all electrochemical reactions, including the parasitic HER. This effect is visually captured in Fig. 14(b), where the Coulombic Efficiency dips transiently to its lowest point of approximately 58% during cycle 4. However, a detailed examination of the discharge capacity uncovers a persistent challenge. While the system stabilizes kinetically, accessible capacity continues to decrease. Throughout the initial phase, the discharge capacity declines from approximately 13.8 A h in cycle 1 to approximately 11.8 A h in cycle 3. Following the thermal ramp to 40 °C, this downward trend persists, albeit at a diminished rate, decreasing from about 10 A h at cycle 5 to roughly 7.5 A h by cycle 15. This gradual capacity fade, despite an improvement in Coulombic Efficiency (to approximately 87%), suggests that while the kinetics of reversible iron plating are enhanced, an ongoing irreversible loss of active material or a proton imbalance persists, necessitating rigorous management. Simultaneously, the voltaic efficiency (VE) shows a positive response to the temperature increase, rising from a baseline of around 64% to maintain a steady ~70% during the warm phase, a change directly attributable to the fivefold increase in the diffusion coefficient. The combination of recovering CE and enhanced VE leads to a net improvement in energy efficiency (EE), increasing from approximately 40% to nearly 60%.

The electrochemical recovery process is fundamentally supported by the chemical stability demonstrated in the *in situ* monitoring data illustrated in Fig. 15. In Panel (a), a time-resolved analysis of electrolyte pH is presented in relation to a thermal step-change. The negative electrolyte pH reveals pronounced oscillations that are directly linked to the charge–discharge cycles. During the charging phase, protons are consumed in tandem with iron deposition and hydrogen evolution reactions (HER), culminating in a rapid increase in pH. Notably, the amplitude of these pH fluctuations increases after the temperature is raised to 40 °C at hour 110. While pH peaks at 20 °C remain below 2.8, operation at 40 °C results in negolyte pH spikes exceeding 4.0, at times approaching 4.5. In standard iron flow battery operations, a pH level above 3.0 is generally regarded as the threshold for the irreversible precipitation of ferrous hydroxide ($Fe(OH)_2$). Nonetheless, the cell's continuous cycling with enhanced efficiency despite these significant pH excursions indicates that the initial conditioning at 20 °C effectively fostered a resilient electrode morphology less prone to passivation.

The efficacy of the active hydrogen management system is quantitatively analyzed in Fig. 15(b), which shows the current drawn by the hydrogen recombination cell. Throughout the initial 20 °C phase (0–110 hours), the RC current exhibits significant, erratic spikes that frequently exceed 250 mA. This behavior aligns with the substantial excess charge capacity observed in Fig. 14(a), affirming that the initial low efficiency was primarily driven by vigorous hydrogen generation. Importantly, the RC current profile undergoes a notable transformation upon increasing the temperature to 40 °C. Although the kinetic rate of HER is theoretically accelerated at elevated temperatures, the RC current shows a distinct decay, with peak currents steadily declining from approximately 400 mA to below 200 mA by the end of the experiment. This inverse relationship is critically significant: as the Coulombic efficiency in the main cell improves, the demand on the recombination cell declines. This observation confirms a stabilizing effect where the active iron surface becomes less catalytic toward HER over time. These findings highlight a crucial operational consideration for future scalability. While the soft-start protocol has effectively mitigated initial failures, the ongoing capacity fade and dependence on the recombination cell underscore the necessity for a robust pressure balance system to manage HER stability at elevated temperatures. Maintaining an accurate pressure differential is essential to ensure efficient hydrogen capture and re-dissolution, thereby preventing gas lock in the system. Furthermore, while this study employed the recombination cell as a monitoring device, its performance characteristics, particularly its reaction kinetics and efficiency limits

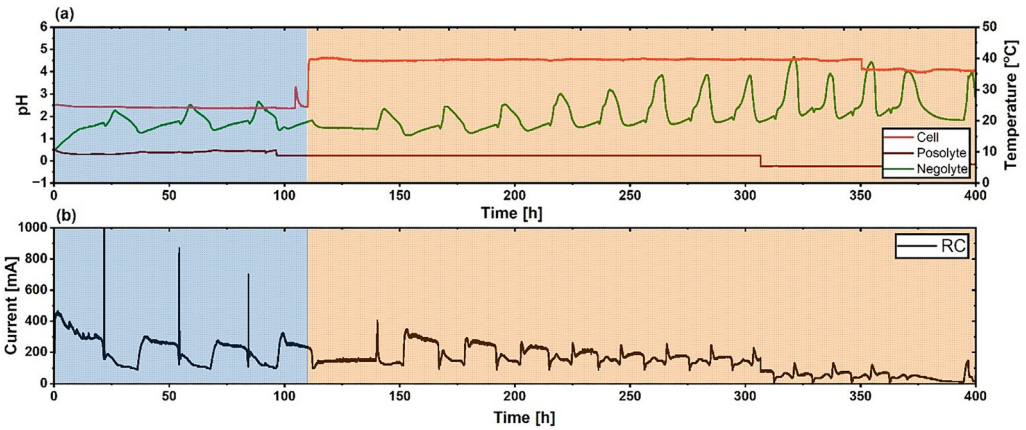

Fig. 15 *In situ* chemical stability monitoring during extended CCCV cycling. (a) Real-time profile of negolyte pH over the 400-hour test duration. (b) The recombination cell current profile over time serves as a proxy for hydrogen evolution rates. The data corresponds to the high-capacity experiment detailed in Fig. 14, illustrating the system's resilience to pH excursions and the stabilization of parasitic currents following the thermal ramp to 40 °C.

under varying current densities, should be examined independently to optimize the overall system energy balance.

Conclusion & future scope

This study systematically investigated the operational performance, stability, and constraints of an all-iron redox flow battery (IRFB) as a function of temperature. Through a combination of half-cell electrochemical analysis and full-cell cycling, it has been demonstrated that thermal management is critical to optimizing performance and extending the operational lifetime of this promising energy storage technology.

The electrochemical characterization confirmed that elevated temperatures significantly enhance reaction kinetics. Notably, the diffusion coefficient of the Fe^{2+} ion increased nearly fivefold between 20 °C and 80 °C, and the morphology of the iron deposit became more crystalline. However, a key finding from the half-cell analysis was the identification of a kinetic trade-off: the coulombic efficiency of the iron plating/stripping process peaked at approximately 71% at 30 °C before declining at higher temperatures, indicating that the parasitic hydrogen evolution reaction (HER) becomes the dominant kinetic effect above this threshold.

In the full-cell system, this trade-off was successfully managed by an integrated hydrogen recycling loop, which was essential for preventing cell failure due to precipitation at elevated temperatures. The full-cell cycling tests identified an optimal operating temperature of 40 °C, which provided the best balance between the enhanced voltaic efficiency from improved kinetics and the high, stable coulombic efficiency maintained by the rebalancing system. To address the challenge of high initial hydrogen losses, a novel ''soft start'' protocol was developed, which involved conditioning the cell at 20 °C before ramping to the 40 °C operating temperature. This strategy proved highly effective, more than doubling the battery's stable operational lifetime to over 80 cycles. Under these optimized conditions, the battery achieved a maximum coulombic efficiency of 94%, a voltaic efficiency of 63%, and an energy efficiency of 60%. The extended CCCV validation demonstrates that the soft-start protocol facilitates stable iron nucleation while keeping the system safely within the acidic regime during the initial cycling phase, despite the significant hydrogen evolution reaction (HER). Upon transitioning to 40 °C, the cell enters a more dynamic acid–alkaline fluctuation range, yet it retains chemical stability due to the electrode's conditioned surface. The improvement in coulombic efficiency (CE), combined with a decreasing RC current demand, indicates that parasitic hydrogen formation becomes less prominent as cycling progresses. Overall, while this strategy effectively manages pH drift and HER, achieving long-term capacity stability will necessitate a more stringent control of proton balance and hydrogen handling at the acidic–alkaline interface.

While this work establishes a viable operational strategy for enhancing IRFB performance, several avenues for future research are apparent. A more granular understanding of the gas management dynamics is crucial. Future research should focus on integrating advanced operando and *in situ* diagnostic techniques to deepen understanding of the complex physicochemical phenomena in iron-based redox flow battery systems. Furthermore, incorporating *in situ* analytical tools, such as mass flow meters, level sensors, and gas chromatography (GC), would enable more accurate quantification of hydrogen generation, recombination, and crossover phenomena. A primary limitation identified at higher temperatures is material stability; thus, the development and testing of more thermally robust ion-exchange membranes capable of operating reliably above 50 °C is a critical next step. Finally, building upon the thermal baseline established here, future studies could explore synergistic improvements through advanced materials, such as alternative electrode architectures or novel electrolyte additives designed to further suppress HER at elevated temperatures.

Conflicts of interest

The authors declare no conflicts of interest.

Acknowledgements

The authors gratefully acknowledge Dr Nataliya Roznyatovskaya for her valuable guidance, insightful discussions, and technical assistance regarding the cyclic voltammetry (CV) measurements. Sincere thanks are also extended to Mr Martin Kastner for his essential support and expertise in developing the temperature-control system used in this study.

References

1 U.S. Energy Information Administration, Annual Energy Outlook 2023, 2023.
2 International Renewable Energy Agency (IRENA), World Energy Transitions Outlook 2023, 2023.
3 M. H. An, L. Liu and J. M. Tarascon, Electrical energy storage for the grid: a battery of choices, *Science*, 2011, **334**, 928–935.
4 K. Zang, J. A. Brehm, A. T. Ntica, C. L. Richard and G. D. Schweitzer III, Smart grid and energy storage: a review, *Energy*, 2018, **161**, 391–401.
5 A. Z. Weber, M. M. Mench, J. P. Meyers, P. N. Ross, J. T. Gostick and Q. Liu, Redox flow batteries: a review, *J. Appl. Electrochem.*, 2011, **41**, 1137–1164.
6 W. Wang, Q. Luo, B. Li, X. Wei, L. Li and Z. Yang, Recent progress in redox flow battery research and development, *Adv. Funct. Mater.*, 2013, **23**, 970–986.
7 P. Alotto, M. Guarnieri and F. Moro, Redox flow batteries for the storage of renewable energy: a review, *Renewable Sustainable Energy Rev.*, 2014, **29**, 325–335.
8 F. Roth, J. Noack and M. Skyllas-Kazacos, in *Flow Batteries: From Fundamentals to Applications*, ed. F. Roth, J. Noack and M. Skyllas-Kazacos, Wiley, 2023, vol. 1, pp. 29–51.

9 J. Noack, N. Roznyatovskaya, T. Herr and P. Fischer, The chemistry of redox-flow batteries, *Angew. Chem., Int. Ed.*, 2015, **54**, 9776–9809.
10 G. L. Soloveichik, Flow batteries: current status and trends, *Chem. Rev.*, 2015, **115**, 11533–11558.
11 M. C. Argyrou, P. Christodoulides and S. A. Kalogirou, Energy storage for electricity generation and related processes: Technologies appraisal and grid scale applications, *Renewable Sustainable Energy Rev.*, 2018, **94**, 804–821.
12 M. Ulaganathan, V. Aravindan, Q. Yan, S. Madhavi, M. Skyllas-Kazacos and T. M. Lim, Recent advancements in all-vanadium redox flow batteries, *Adv. Mater. Interfaces*, 2016, **3**, 1500309.
13 L. W. Hruska and R. F. Savinell, Investigation of Factors Affecting Performance of the Iron-Redox Battery, *J. Electrochem. Soc.*, 1981, **128**, 18–25.
14 S. Belongia, X. Wang and X. Zhang, Progresses and perspectives of all-iron aqueous redox flow batteries, *Adv. Funct. Mater.*, 2024, **34**, 2302077.
15 S. Selverston, E. Nagelli, J. Wainright and R. Savinell, All-Iron Hybrid Flow Batteries with In-Tank Rebalancing, *J. Electrochem. Soc.*, 2019, **166**, A1725–A1731, DOI: 10.1149/2.0281910jes.
16 S. Zhang, *et al.*, All-soluble all-iron aqueous redox flow batteries: Towards sustainable energy storage, *Energy Storage Mater.*, 2025, **75**, 104004.
17 K. Gong, X. Ma, K. M. Conforti, R. J. Kuttner and F. Wang, A high-performance all-iron flow battery, *Energy Environ. Sci.*, 2015, **8**, 2941–2945.
18 J. O. 'M. Bockris and A. K. N. Reddy, *Modern Electrochemistry 2A: Fundamentals of Electrodes*, Springer, 2000.
19 E. Gileadi, *Physical electrochemistry: fundamentals, techniques, and applications*, John Wiley & Sons, 2011.
20 Y. Kim, *et al.*, An iron-based redox flow battery with a high cell voltage and energy efficiency, *Adv. Energy Mater.*, 2017, **7**, 1602534.
21 D. Bevers, *et al.*, The Pourbaix diagram of iron in chloride-containing solutions, *Corros. Sci.*, 2019, **157**, 344–353.
22 M. Pourbaix, *Atlas of electrochemical equilibria in aqueous solutions*, National Association of Corrosion Engineers, 1974.
23 B. Kurzweil, in *Electrochemical Energy Storage for Renewable Sources and Grid Balancing*, Elsevier, 2015, pp. 269–307.
24 M. Genovese, *et al.*, A perspective on metal-based additives for suppressing hydrogen evolution in aqueous batteries, *J. Mater. Chem. A*, 2020, **8**, 16147–16164.
25 C. Sun, *et al.*, suppressing hydrogen evolution reaction in an all-iron flow battery by using electrolyte additives, *J. Power Sources*, 2019, **438**, 227033.
26 C. Sun and H. Zhang, Critical review on the research and development of iron-based flow batteries, *ChemSusChem*, 2021, **15**, e202101798.
27 E. S. Lee, *et al.*, Effect of additives on the electrochemical performance of an all-iron hybrid redox flow battery, *Electrochim. Acta*, 2018, **271**, 250–257.
28 J. Noack, M. Wernado, N. Roznyatovskaya, J. Ortner and K. Pinkwart, Studies on Fe/Fe Redox Flow Batteries with Recombination Cell, *J. Electrochem. Soc.*, 2020, **167**, 160527.
29 J. Zhang, L. Li, Z. Wu, J. Zhao and X. Qiu, Effects of operating temperature on the performance of vanadium redox flow batteries, *J. Power Sources*, 2015, **294**, 14–22.
30 A. Tang, *et al.*, A study of the thermal properties of vanadium electrolytes for redox flow battery applications, *J. Power Sources*, 2011, **196**, 8909–8914.
31 M. Skyllas-Kazacos and C. Menictas, The vanadium redox battery: ten years of development, *J. Electrochem. Soc.*, 2012, **159**, A1277.
32 I. Roe, C. Menictas and M. Skyllas-Kazacos, A review of membrane selection and manufacturing for vanadium redox flow batteries, *J. Energy Storage*, 2016, **5**, 127–150.
33 M. Vijayakumar, *et al.*, The role of V(v) precipitation on the performance of the vanadium redox flow battery, *J. Power Sources*, 2009, **190**, 565–571.
34 Z. Wei, T. Zhao, S. L. Zhao, L. F. Zeng and L. Wei, The effects of temperature and electrolyte flow rate on the performance of a zinc–bromine flow battery, *Appl. Energy*, 2018, **229**, 107–115.
35 R. M. Darling, *et al.*, Electrolyte Lifetime in Aqueous Organic Redox Flow Batteries: A Critical Review, *Chem. Rev.*, 2020, **120**, 7584–7633.
36 J. Winsberg, T. Hagemann, T. Janoschka, M. D. Hager and U. S. Schubert, Redox-flow batteries: from molecules to systems, *Angew. Chem., Int. Ed.*, 2017, **56**, 686–711.
37 B. S. Jayathilake, E. J. Plichta, M. A. Hendrickson and S. R. Narayanan, Improvements to the Coulombic Efficiency of the Iron Electrode for an All-Iron Redox-Flow Battery, *J. Electrochem. Soc.*, 2018, **165**, A1630–A1638.
38 A. Rana, Md. A. Faisal, K. Roy, J. H. Nguyen, S. Paul and J. E. Dick, How the Kinetic Balance Between Charge-Transfer and Mass-Transfer Influences Zinc Anode Stability: An Ultramicroelectrode Study, *Small Methods*, 2025, **9**, 2401021.
39 W. J. Lorenz, H. D. Hermann, N. Wüthrich and F. Hilbert, The Formation of Monolayer Metal Films on Electrodes, *J. Electrochem. Soc.*, 1974, **121**, 1167.
40 Q. Zhang and Y. Song, Electrochemical analysis of electrolyte temperature and composition for all-iron redox flow battery, *Int. J. Green Energy*, 2022, **19**, 1285–1289.
41 J. Noack, M. Berkers, J. Ortner and K. Pinkwart, The Influence of Some Electrolyte Additives on the Electrochemical Performance of Fe/Fe^{2+} Redox Reactions for Iron/Iron Redox Flow Batteries, *J. Electrochem. Soc.*, 2021, **168**, 040529.
42 S. M. Selverston, Iron-Based Flow Batteries: Improving Lifetime and Performance, PhD thesis, University of California, 2017.
43 I. Gimenez-Garcia, M. Tabuyo-Martinez, P. Boillat, R. R. Jacquemond, A. Mularczyk and A. Forner-Cuenca, Polarization contrast neutron imaging enables operando visualization of iron plating in redox flow batteries, *ChemRxiv*, 2025.

44 E. B. Boz, A. Bondre, R. de Bruijne and A. Forner-Cuenca, Conductive Polymer Coatings Control Reaction Selectivity in All-Iron Redox Flow Batteries, *Adv. Mater.*, 2025, **37**, 2414596, DOI: 10.1002/adma.202414596.
45 K. Köble, A. Ershov, K. Duan, M. Schilling, A. Rampf, A. Cecilia, T. Faragó, M. Zuber, T. Baumbach and R. Zeis, Insights into the hydrogen evolution reaction in vanadium redox flow batteries: A synchrotron radiation-based X-ray imaging study, *J. Energy Chem.*, 2024, **91**, 132–144.
46 G. K. Vadlamudi and A. Chatterjee, Dynamic interplay between electrochemical Zn deposition and hydrogen evolution reaction in low pH environments, *J. Power Sources*, 2025, **657**, 238162.